PNAS
www.pnas.org

Supplementary Information for

Biologically Inspired Flexible Photonic Films for Efficient Passive Radiative Cooling

Haiwen Zhang, Kally Chein Sheng Ly, Xianghui Liu, Zhihan Chen, Max Yan, Zilong Wu, Xin Wang, Yuebing Zheng, Han Zhou and Tongxiang Fan

Han Zhou and Tongxiang Fan
Email: hanzhou_81@sjtu.edu.cn; txfan@sjtu.edu.cn

This PDF file includes:

Other supplementary materials for this manuscript include the following:

www.pnas.org/cgi/doi/10.1073/pnas.2001802117

Supplementary Text

1. Characterization and experiments

Characterization of biological specimens and Bio-RC films. Images of the biological samples and bioinspired radiative cooling films were photographed by HUAWEI Mate10 (visible) and FLIR T630c (MIR) cameras. A field emission scanning electron microscope (FESEM, FEI NOVA NanoSEM 230) was used to reveal more details of scales. In addition, the surface micro-topography of the Bio-RC film was measured by an environment control scanning probe microscope (Seiko, Nanonavi E-Sweep). The cross sections of the specimen fluffs were characterized by a transmission electron microscope (TEM, FEI Tecnai G2 spirit Biotwin). Optical characterization was conducted in the range from visible to MIR wavelengths. For the visible and NIR spectra range, the reflectivity measurements of forewings with and without fluffs were conducted by microspectrograph (Ideaoptics, FX4000 fiber spectrometer for the range of 200–1100 nm; NIR1700 near-infrared spectrometer for the range of 900–1700 nm). The reflectivity measurements of bioinspired hybrid films with metasurfaces were determined for the range of 300–2500 nm by a UV/VIS/NIR spectrophotometer (PerkinElmer, Lambda 950). For the MIR spectra, a Fourier transform infrared (FT-IR) spectrometer (Thermo Scientific, Nicolet 6700). The reflectivity and transmittance were measured by a gold integrating sphere (Peak technologies).

Refractive index measurements were taken for Al_2O_3-PDMS film without photonic structures using Spectral ellipsometer (V-VASE, J.A. Woollam Co., Inc.) in the visible-NIR wavelength range (0.3–2.5 μm). In the MIR wavelength range (2.5–16 μm), the refractive index was measured by Infrared spectral ellipsometer (IR-VASE, J.A. Woollam Co., Inc.).

Mechanical strength measurement of the Bio-RC film was carried out at room temperature using dynamic thermo-mechanical analyzer (DMA, Q800, TA Instruments). The contact angles of water/air droplet were measured by drop shape analyzer (DSA 100, KRUSS). Distilled water (8 μL, with a surface tension of 72.0−73.0 mN m^{-1}) was used as the probe liquid.

Wetting and drying experiment. The ethanol solution with concentration of 70% was dripped onto the forewings of *N. gigas*. The fluffs on the elytra gradually changed from a wetting state to a drying state by evaporation. The reflectivity of the fluffs was characterized using a microspectrograph (NOVA, Ideaoptics).

Finite-difference time-domain simulations. Full-wave simulations were conducted by FDTD Solutions (V8.21.1882, Lumerical Co.Ltd) to simulate the reflectivity and the absorptivity/emissivity. Specifically, for the forewings of longicorn beetle specimens, the microstructural details of the fluff cover were recreated by abstract models, which are supposed to be tightly arrangement. Realistic optical properties of the chitin-protein complex (refractive index ~1.56, obtained from spectroscopic measurements) were assigned to the fluff structures. For the Bio-RC films, the refractive index data was obtained from the actual measurement and the refractive index database. The reflectivity was

calculated by averaging the results for TE- and TM-polarized light to account for the non-polarized incident light in experiments.

Thermodynamics and radiative cooling performance demonstrations. Thermodynamics measurements were conducted in a vacuum chamber (Janis ST-100). Before and after fluffs removal, the forewings cut from the longicorn beetle specimens were placed in the chamber both in normal and vacuum conditions. In order to decrease thermal conduction, the specimen was attached to a block of polystyrene foam. The vacuum experiments were conducted at a pressure below 0.001 Pa to minimize convective heat transfer. We utilized a high-power Xenon lamp (X350) to simulate solar radiation with a power of ~ 800W/m^2. Meanwhile, the lamp was linked with an automatic shutter, which accurately controlled the switch of the radiation source. The radiation source was turned on for 150s and then turned off with the control of the shutter. The temperature variations of the specimens were recorded to obtain a temporal temperature profile with the infrared thermal imaging camera (FLIR T630c). We also used research IR software to analyze the statics to determine the rise and decay time constants and the steady-state temperature. The passive radiative cooling performance of the Bio-RC film were conducted in late May. A solar power radiation meter (TES1333, TES) has the spectral response ranging from 400 to 1100nm was used to record the local solar radiation. The relative humidity and ambient temperature were measured by a hygrothermograph (A200-TH, HUATO). The real-time temperature was measured by a multi-channel datalogger (GL240, GRAPHTEC Corporation). The radiative cooling power was measured by a computer-controlled metal ceramic heater. According to the dynamic temperature compensation mechanism, the cooling power can be calculated from the power consumed in heating the Bio-RC film up to the ambient temperature.

2. Calculations of gradual index (GRIN) change

Considering that the MIR wavelength is several times larger than the size of the dual-scale triangular cross-section, we applied a second-order approximation to calculate the effective refractive index of a given filling factor by effective medium theory. When the MIR light illuminates the simplified model (Fig. S4*A*), the corresponding equations used to calculate the data shown in Figs. S4*B*–*D* are:(1)

Second-order approximation:

$$\varepsilon_{TM}^{(2)}(z) = \varepsilon_{TM}^{(0)}(z)\left[1 + \frac{\pi^2}{3}\left(\frac{\Lambda}{\lambda}\right)^2 f^2(z)[1-f(z)]^2 \frac{(\varepsilon_s-\varepsilon_i)^2}{\varepsilon_0 \varepsilon_{TE}^{(0)}(z)}\right] \quad (1)$$

$$\varepsilon_{TM}^{(2)}(z) = \varepsilon_{TM}^{(0)}(z)\left[1 + \frac{\pi^2}{3}\left(\frac{\Lambda}{\lambda}\right)^2 f^2(z)[1-f(z)]^2 (\varepsilon_s-\varepsilon_i)^2 \frac{\varepsilon_{TE}^{(0)}(z)}{\varepsilon_0}\left(\frac{\varepsilon_{TM}^{(0)}(z)}{\varepsilon_i \varepsilon_s}\right)^2\right] \quad (2)$$

Zeroth-order approximation:

$$\varepsilon_{TE}^{(0)}(z) = f(z)\varepsilon_s + [1-f(z)]\varepsilon_i \quad (3)$$

$$\frac{1}{\varepsilon_{TM}^{(0)}(z)} = \frac{f(z)}{\varepsilon_s} + \frac{1-f(z)}{\varepsilon_i} \quad (4)$$

$$\frac{\Lambda}{\lambda} < \frac{1}{max\,[n_s, n_i]} \quad (5)$$

where $f(z) = \frac{a(z)}{\Lambda}$. The equation represents the zeroth-order estimation of the effective permittivity for TE (aligned parallel with hairs) and TM (perpendicular to hairs) incident light. The filling factor $f(z)$ represents the proportion of the triangular section marked by its z position. Λ represents the width of the triangular hair cross section and λ is the MIR wavelength of interest. The permittivity of the fluffs and air are ε_s and ε_i, respectively.

3. Thermodynamic experiment and calculations

In the thermodynamic experiments, the temperature variations of forewings were caused by the heat transfer process, including heat absorption and radiation and heat convection in the air, which can be represented by the following equation:(2)

$$mC\frac{dT}{dt} = Q_{light} + Q_{surr} - Q_{rad} - Q_{conv}$$
$$= \alpha G_{light} A_s + \alpha' \sigma T_{surr}^4 A_s - \varepsilon \sigma T^4 A_s - hA_s(T - T_{surr}) \quad (6)$$

$\boldsymbol{mC\frac{dT}{dt}}$**:** Representing the total rate of change of stored heat energy. *C* is the specific heat for chitin, which is 1.56 $Jg^{-1}\,K^{-1}$ and *m* is the weight of the specimen.

$\boldsymbol{Q_{light} = \alpha G_{light} A_s}$**:** Representing the energy of the light source absorbed by the forewings. Here, α is defined as the average absorptivity over the spectrum of the light. G_{light} represents the light intensity incident onto the forewings. A_s is the surface area illuminated by light.

$\boldsymbol{Q_{surr} = \alpha' \sigma T_{surr}^4 A_s}$**:** Expressed as the energy obtained by thermal radiation of the surrounding environment to the surface of the forewings. Here, α' is the average absorptivity of the external environment. σ refers to the Stefan-Boltzmann constant. T_{surr} is the temperature of the surrounding environment.

$\boldsymbol{Q_{rad} = \varepsilon \sigma T^4 A_s}$**:** Expressed as the energy radiated by the forewings at the temperature of T. ε is the average emissivity with and without the fluffs.

$\boldsymbol{Q_{conv} = hA_s(T - T_{surr})}$ **:** Described as the energy transferred by heat convection. Here, *h* represents heat transfer coefficient.

Since the forewings were attached to a block of polystyrene foam in the chamber, the heat

conduction was neglected. In order to investigate the variation of temperature with time, a series of calculations and simplifications were carried out, as follows:

$$Q_{rad} = \varepsilon\sigma T^4 A_s = \varepsilon\sigma A_s (T - \bar{T} + \bar{T})^4 = \varepsilon\sigma A_s \bar{T}^4 (\frac{T - \bar{T}}{\bar{T}} + 1)^4$$

$$\approx \varepsilon\sigma A_s \bar{T}^4 \left(4\frac{T-\bar{T}}{\bar{T}} + 1\right) = 4\varepsilon\sigma A_s \bar{T}^3 T - 3\varepsilon\sigma A_s \bar{T}^4 \quad (7)$$

where $\bar{T}$ is the average temperature of the maximum and minimum values.

$$\begin{aligned} mC\frac{dT}{dt} &= \alpha G_{light} A_s + \alpha' \sigma T_{surr}^4 A_s - 4\varepsilon\sigma A_s \bar{T}^3 T + 3\varepsilon\sigma A_s \bar{T}^4 - hA_s(T - T_{surr}) \\ &= (\alpha G_{light} A_s + \alpha' \sigma T_{surr}^4 A_s + 3\varepsilon\sigma A_s \bar{T}^4 + hA_s T_{surr}) - (4\varepsilon\sigma A_s \bar{T}^3 + hA_s)T \\ &= B - AT \end{aligned} \quad (8)$$

where $B = \alpha G_{light} A_s + \alpha' \sigma T_{surr}^4 A_s + 3\varepsilon\sigma A_s \bar{T}^4 + hA_s T_{surr}$, and $A = 4\varepsilon\sigma A_s \bar{T}^3 + hA_s$. Therefore, the above equation can be transformed into:

$$\frac{mC}{B-AT} dT = dt \ (B - AT \neq 0) \quad (9)$$

The variation of temperature with time can be obtained by integrating both sides of the equation:

$$\mathrm{T} = \begin{cases} -\frac{1}{A}\exp\left(-\frac{At}{mC}\right) + \frac{B}{A} + R_1 \ (B - AT > 0) \\ \frac{1}{A}\exp\left(-\frac{At}{mC}\right) + \frac{B}{A} + R_2 \ (B - AT < 0) \end{cases} \quad (10)$$

where R_1 and R_2 are both specific real numbers. While the equations of time constants can be obtained from the above equation in air (τ) and in vacuum (τ'), respectively. The difference between the two conditions originates from the existence of heat convection. The equations can be described as follows:

$$\tau = \frac{mC}{A} = \frac{mC}{4\varepsilon\sigma A_s \bar{T}^3 + hA_s} \quad (11)$$

$$\tau' = \frac{mC}{A} = \frac{mC}{4\varepsilon\sigma A_s \bar{T}^3} \quad (12)$$

The corresponding average emissivity ε can be obtained in the context of given the other parameters from the equation (12).

During the whole process that the forewings with/without fluffs illuminated by the source, the

changes in energy caused by thermal radiation (ΔQ_{rad}) and convection (ΔQ_{conv}) are represented by the following equations:

$$\Delta Q_{rad} = \varepsilon \sigma A_s (T_{max}^4 - T_{min}^4) \quad (13)$$

$$\Delta Q_{conv} = hA_s (T_{max} - T_{min}) \quad (14)$$

The results for the forewing before and after the fluffs removal are summarized in Table S1. Assuming the fluffs cover approximately 50% of the forewing, the emissivity of only fluffs (ε_f) can be described as:

$$\varepsilon_{f+b} = 0.5\varepsilon_f + 0.5\varepsilon_b \quad (15)$$

where ε_{f+b} and ε_b are the emissivity of the forewing before and after the fluffs removed.

According to the equation, we derived that the emissivity of the fluffs (ε_f) is 0.914. The fluffs can enhance the average MIR emissivity by (0.914−0.824)/0.824=10.92%.

4. Measurements and calculations of refractive index

According to the Maxwell-Garnett effective medium approximation,(3, 4) the dielectric function for doped PDMS matrix is determined as follows:

$$\varepsilon(\lambda) = \varepsilon_m + 3f\varepsilon_m \left[\frac{\frac{\varepsilon_p - \varepsilon_m}{\varepsilon_p + 2\varepsilon_m}}{1 - f\frac{\varepsilon_p - \varepsilon_m}{\varepsilon_p + 2\varepsilon_m}} \right] \quad (16)$$

where ε_m and ε_p are the dielectric functions of matrix and particles, f is the volume fraction of particles. The conversions of dielectric constant to refractive index are as follows:

$$\varepsilon_r(\lambda) = n^2 - k^2 \quad (17)$$

$$\varepsilon_i(\lambda) = 2nk \quad (18)$$

The theoretical calculation of the refractive index of the Al_2O_3-PDMS hybrid film is almost the same as the experimental measurement (Fig. S7*A*), which indicates that the two ingredients are mixed evenly. Besides, under irradiation with lights of different wavelengths such as 0.72 μm in vis-NIR region and 10 μm in MIR region (Figs. S7*B* and *C*), the refractive index range with the volume fraction of Al_2O_3 particles at different wavelengths can be estimated by using the abovementioned equations.

5. Calculations based on diffusion theory and measurements of transmissivity

We experimentally extracted the photon mean free path (l^*) to illuminate the behavior of sunlight

incident on the Al_2O_3-PDMS hybrid film based on a diffusion theory.(5, 6) The transmissivity *T* of a film related to its thickness *L* can be expressed as follows:

$$T = \frac{1+Z_e}{\left(\frac{L}{l^*}\right)+2Z_e} \tag{19}$$

where Z_e is the extrapolation length ratio which is a sample-dependent number on the order of unity, and is related to the transmittance as a function of the angle θ from the surface normal. Z_e is calculated from the angular probability distribution of transmitted light as follows:

$$\frac{P(\mu)}{\mu} = \frac{(z_e+\mu)}{\frac{1}{2}Z_e+\frac{1}{3}} \tag{20}$$

where μ=cos (θ), and $\int P(\theta)\sin\theta d\theta = \int P(\mu)d\mu$ =1.

In order to determine the extrapolation length ratio Z_e, Fresnel law need to be applied, the rate of incidence:

$$r_{e-s} = \frac{n_e\cos(\theta_e)-n_i\cos(\theta_i)}{n_e\cos(\theta_e)+n_i\cos(\theta_i)} \tag{21}$$

$$r_{e-p} = \frac{n_i\cos(\theta_e)-n_e\cos(\theta_i)}{n_i\cos(\theta_e)+n_e\cos(\theta_i)} \tag{22}$$

$$r_{i-s} = \frac{2n_e\,cos(\theta_e)}{n_e\cos(\theta_e)+n_i\cos(\theta_i)} \tag{23}$$

$$r_{i-p} = \frac{2n_e\,cos(\theta_e)}{n_i\cos(\theta_e)+n_e\cos(\theta_i)} \tag{24}$$

At the wavelength λ of 0.72 μm, which lies above/below which 50% of solar intensity. The refractive indexes of air and the Bio-RC film at the wavelength of 0.72 μm are $n_1 = 1, n_2 = 1.3973$, θ_e is ranging from 0 to $\frac{\pi}{2}$. When θ_e reaches up to the maximum, which is $\frac{\pi}{2}$, according to $n_e\,sin(\theta_e) = n_i sin\,(\theta_i)$, the value of θ_i is 0.7976. For a photon striking the interior boundary at an angle μ_i, $R(\mu_i)$ represents the total boundary reflectivity by incoherently summing over all multiple reflections, which can be shown as follows:

$$R(\mu_i) = \frac{R_e+R_i-2R_eR_i}{1-R_eR_i} \tag{25}$$

where *R* is the Fresnel reflectivity for interface at the appropriate angle by Snell's law. The reflectivity moments are defined as

$$R_n = \int_0^1 (n+1)\mu^n R(\mu) d\mu \quad (26)$$

Z_e can be calculated by:

$$Z_e = \frac{2}{3}\frac{1+R_2}{1-R_1} \quad (27)$$

The calculated Z_e is depicted in Figs. S10*A*−*C*. The photon mean free path l^* can be calculated by the extrapolation length ratio Z_e, which is ranging from ~3 μm to ~18 μm for the measured wavelengths hint at the interaction between different wavelengths of light and the Bio-RC film. For example, the blue wavelengths have the photon mean free path of ~3 μm, which would be efficiently scattered by the Al_2O_3 spherical particles. When the wavelength is longer, the photon mean free path l^* is also increasing, which implies less well-scattered by the ceramic particles and penetrate deeper into the Bio-RC film. This is evident in the transmission spectra that the Bio-RC film shows a higher transmissivity for longer solar wavelengths (Fig. S10*D*). In addition, the measured transmissivity decreases with the increasing of the film thickness. According to Equation (19), the theoretically predicted transmissivity of the Bio-RC films calculated by the Z_e and l^* for λ = 0.72 μm is consistent with the experimental data (Fig. S10*E*), which indicates the accuracy of the calculations based on diffusion theory. Furthermore, it provides an easy and effective approach to achieve the specific transmissivity by adjusting the thickness of the film.

6. Measured optical properties with the thickness of the film

The transmissivity and reflectivity spectra of Al_2O_3-PDMS hybrid films with different thicknesses were measured and simulated. The results were shown in Fig. S10 and Fig. S12 in Supplementary Information. The detailed explanations are as follows: The MIR emissivity (ε) was calculated based on the MIR reflectance (*r*) and the MIR transmittance (*t*) data according to the Kirchhoff's Law of $\varepsilon = \alpha = 1 - r - t$. The transmittance in the 8–13 μm TASW wavelength range approached zero with the thickness more than 225 μm (Fig. S10*D*). The result revealed that the maximum emissivity $\varepsilon = 1 - r$ was determined by the reflectance. As clearly shown in Fig. S12, the reflectivity in the 8–13 μm was almost unchanged with the increasement of the thickness, indicating that the absorptivity/emissivity spectra of the films were irrelevant to the thickness. In the vis-NIR region, when the thickness decreased, the transmittance increased gradually (Figs. S10*D* and *E*). Thus, the vis-NIR reflectivity gradually decreased with the thickness decreasing (Fig. S12). On the contrary, when the thickness was larger than ~500 μm, the variations of the corresponding reflectivity were not obvious. Based on the analysis, we prefer a relatively thinner Bio-RC film of 500 μm on the consideration of the production cost, synthetic procedures and optical properties. Yet a sample with 500-μm thickness is easier to handle and exhibits more favorable mechanical properties than thinner samples.

7. Calculated radiation cooling power of the Bio-RC film

The energy balance process of the Bio-RC film in radiative cooling process is illustrated in Fig. S16*A*, where P_{rad} is the energy radiated into space, P_{sky} is the atmospheric radiative energy absorbed, P_{solar} is the solar energy absorbed, and $P_{cond-conv}$ represents the non-radiative parasitic losses. According to the conservation of energy, the net cooling power (P_{net}) represents the combined interactions of the previously mentioned energy flows, which can be described as follows:(7)

$$P_{net} = P_{rad}(T_r) - P_{sky} - P_{solar} - P_{cond-conv} \tag{28}$$

Here, considering that the real area of the Bio-RC film is A_r and the radiation temperature is T_r, the thermal radiation power P_{rad} can be calculated by:

$$P_{rad} = \int_0^{+\infty} \int_0^{2\pi} \int_0^{\frac{\pi}{2}} \varepsilon_r(\lambda, \theta, \varphi, T_r)\, I_b(\lambda, T_r) cos(\theta) sin(\theta) d\theta d\varphi d\lambda \tag{29}$$

where $\varepsilon_r(\lambda, \theta, \varphi, T_r)$ is the spectral emissivity. Here, T_r represents the surface temperature. $I_b(\lambda, T_r) cos(\theta)$ represents the intensity of black-body radiations at T_r, which is taken as:

$$I_b(\lambda, T_r) \cos(\theta) = \frac{2hc^2}{\lambda^5} \frac{1}{e^{\frac{hc}{\lambda kT}} - 1} \tag{30}$$

where *h*, *c* and *k* are Planck's constant, velocity of light in vacuum and Boltzmann's constant, respectively. For the engineering calculations, azimuth angle φ and surface temperature T_r on $\varepsilon_r(\lambda, \theta, \varphi, T_r)$ can be neglected. Therefore, the formula (29) can be simplified as follows:

$$P_{rad} = \pi \int_0^{+\infty} \int_0^{\frac{\pi}{2}} \varepsilon_r(\lambda, \theta)\, I_b(\lambda, T_r) sin(2\theta) d\theta d\lambda \tag{31}$$

According to the thermal radiation principles, the absorbed sky radiation can be given by:

$$P_{sky} = \pi \int_0^{+\infty} \int_0^{\frac{\pi}{2}} \alpha_r(\lambda, \theta)\, I_s(\lambda, \theta, T) sin(2\theta) d\theta d\lambda \tag{32}$$

where $\alpha_r(\lambda, \theta)$ refers to the spectral absorptivity of the Bio-RC film and equals to the spectral directional emissivity $\varepsilon_r(\lambda, \theta)$ based on Kirchhoff's law of thermal radiation. The spectral directional radiation power of the sky atmosphere can be described as follows:

$$I_s(\lambda, \theta, T) = \varepsilon_s(\lambda, \theta) I_b(\lambda, T_a) \tag{33}$$

where $\varepsilon_s(\lambda, \theta)$ is the spectral directional emissivity of the sky atmosphere, which can be expressed as:

$$\varepsilon_s(\lambda, \theta) = 1 - [\tau_s(\lambda, 0)]^{1/cos(\theta)} \tag{34}$$

where $\tau_s(\lambda, 0)$ represents the atmospheric transmissivity at vertical direction. T_a is the ambient temperature.

The absorbed solar radiation is defined as P_{solar}, which can be expressed as follows:

$$P_{solar} = \int_0^{+\infty} a_r(\lambda, \theta_{sun}) I_{AM1.5}(\lambda) d\lambda \quad (35)$$

where θ_{sun} is the incident angle of the sunlight impinging on the Bio-RC film, $I_{AM1.5}(\lambda)$ is the AM 1.5 spectrum distribution of the solar radiation intensity varying with the wavelength. The AM 1.5 spectrum profile is shown in Fig. S16*B*.

The non-radiative parasitic losses $P_{cond-conv}$ are quantified by the effective conductive-convective heat transfer coefficient h which can be described as follows:

$$P_{cond-conv} = hA_r(T_a - T_r) \quad (36)$$

Assuming that the Bio-RC film has the average vis-NIR reflectivity of 95% and radiates 96% of the MIR heat, the net radiative cooling power P_{net} gradually increases as the radiation temperature goes up in the case of the non-radiative parasitic losses $P_{cond-conv}$ ignored and the ambient temperature fixed at 30 °C (Fig. S16*C*). In addition, under the abovementioned conditions, the Bio-RC film has the maximum temperature drop of nearly 20 °C when the net cooling power is zero (Fig. S16*D*). Also, the maximum temperature drop of ΔT goes up with the increase of the ambient temperature. Fig. S16*E* indicates the value of P_{net} varying with different radiation and ambient temperatures. A significantly higher net cooling power is achieved with the decrease of the ambient temperature and the increase of the radiation temperature. Taking the non-radiative parasitic losses $P_{cond-conv}$ into consideration, when ΔT is fixed, the net radiative cooling power is dropped with the increase of the effective conductive-convective heat transfer coefficients *h* (Fig. S16*F*).

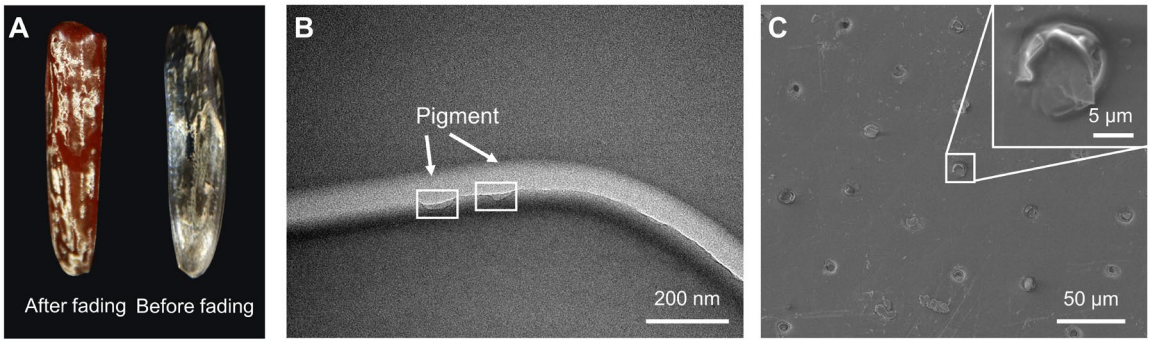

Fig. S1. Morphology of the forewings of the longicorn specimen. (*A*) Optical topography of the forewings before and after fading. After the pigment removal, the fluffs turned to be shining silvery. (*B*) TEM image of the grooves of the fluff deposited by pigmentation to darken the colour. (*C*) SEM image of the forewing after the fluffs removed. The density of fluffs is approximately 25,500 per square centimetre according to the follicle estimation. Inset is the morphology of a hair follicle.

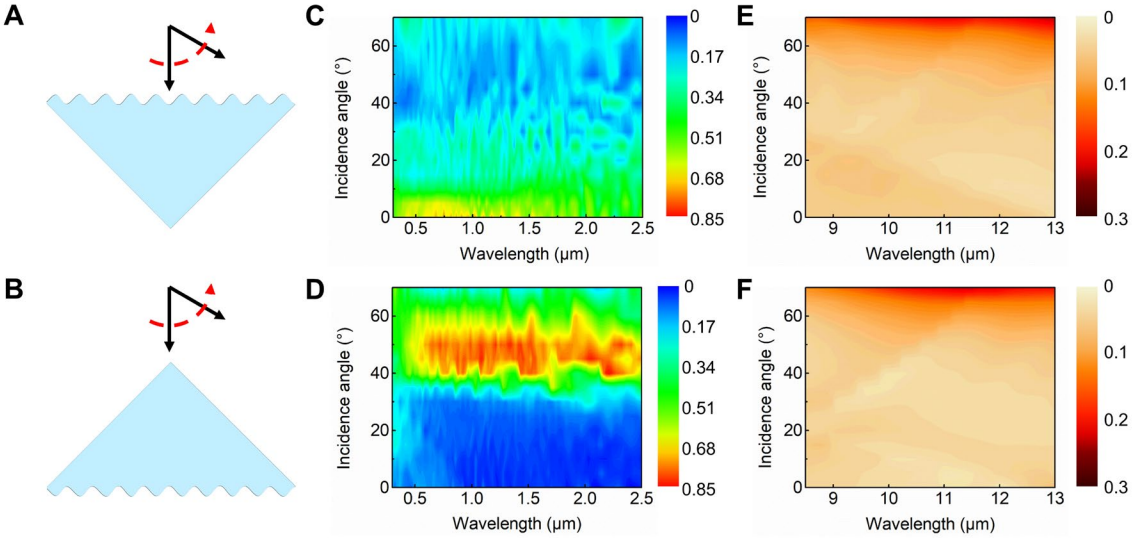

Fig. S2. Simulated optical properties of the fluff. (*A* and *B*) Schematic illustrations of (*A*) the corrugated facet with frills and (*B*) the smooth side facets exposed to light at different angles. (*C* and *D*) Simulated reflectance spectra of the fluff sections with different incident angles in the visible to near infrared (vis-NIR) region. When light impinges on the corrugated frills, total internal reflection occurs at a small angle of incidence. When the smooth facets are exposed to incident light at an angle beyond 36°, total internal reflection generates inside the fluffs. (*E* and *F*) Simulated mid-infrared (MIR) reflectance spectra of (*E*) the corrugated facet and (*F*) the smooth facets at different incident angles ranging from 0° to 70°; both cases remain high MIR emissivity for a wide range of angles.

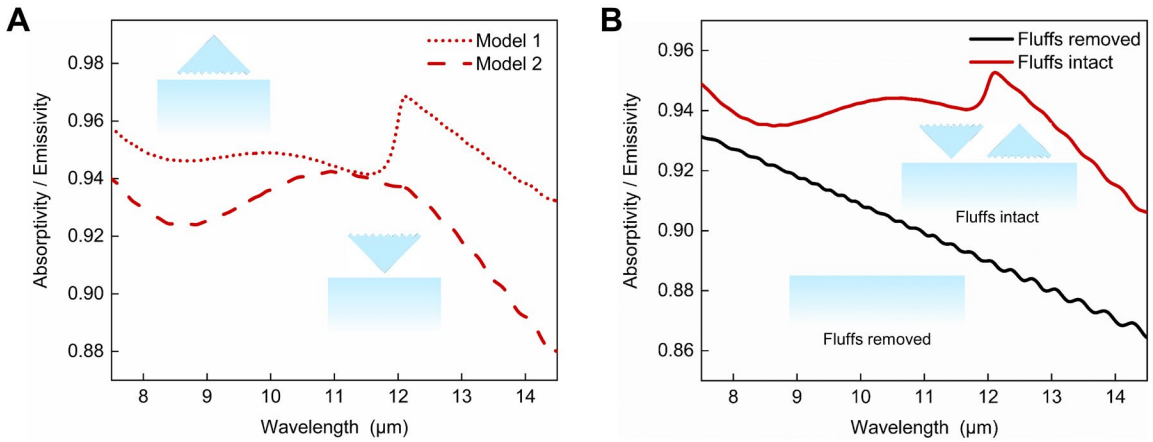

Fig. S3. The effect of the fluff's dual-scale microstructures on the MIR emissivity. (*A*) Simulated values of spectral absorptivity/emissivity of the abstracted fluffs on the elytra for both incident directions and the corresponding the average emissivity over the whole TASW wavelength range. The refractive index of the chitin-protein complex layer is 1.56. (*B*) The MIR absorptivity/emissivity of the forewings before and after fluffs removal simulated at normal incidence. The abstracted section of the forewing with fluffs are composed of the two hierarchical models in (*A*) with the proportion of 1:1.

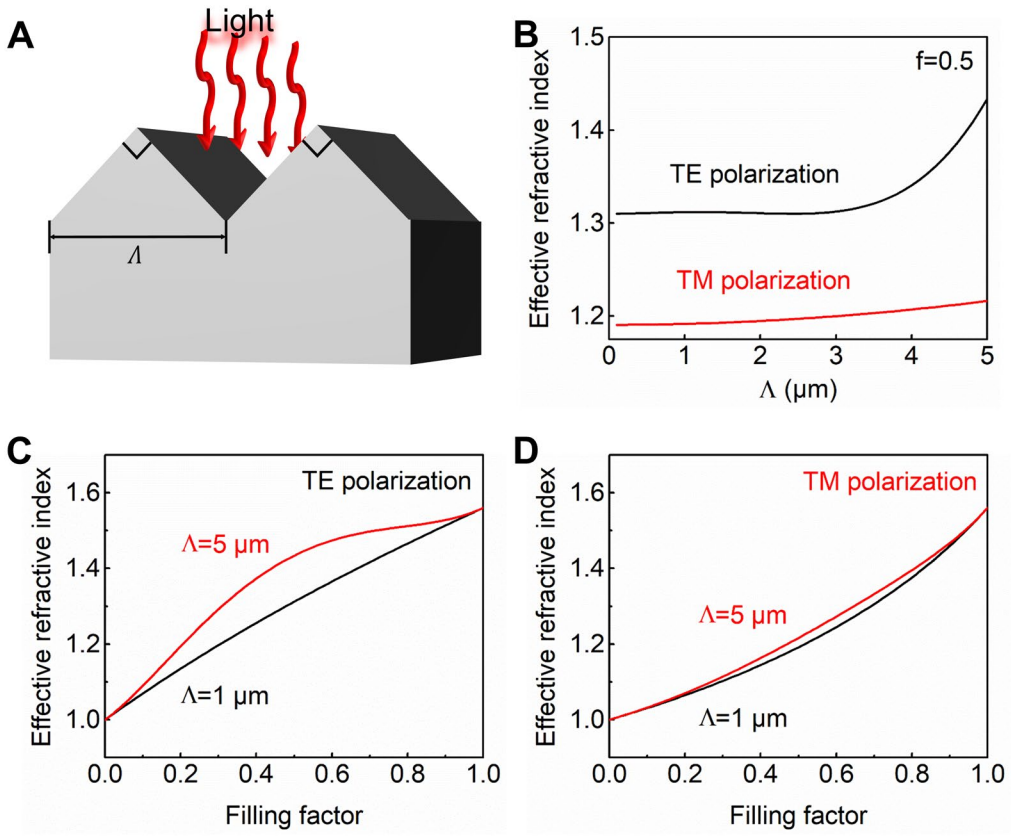

Fig. S4. Calculations of gradual index (GRIN) change. (*A*) Model diagram of an isosceles right triangular section with the width Λ of the bottom edge to approximately represent the corrugate facets (Λ=1 μm) and the integral structure (Λ=5 μm) of the fluff. The incident infrared light impinges on the triangular section which changes the optical effects. (*B*) Effective refractive index with the width Λ ranging from 0.1 μm to 5 μm for different polarizations. The variation magnitude of the effective refractive index in TE polarization is greater than that in TM polarization with the fixed filling factor of 0.5. (*C* and *D*) Effective refractive index of the triangular sections with the filling factor ranging from 0 to 1 in (*C*) TE and (*D*) TM polarizations. The extent of GRIN change is more pronounced with a greater Λ.

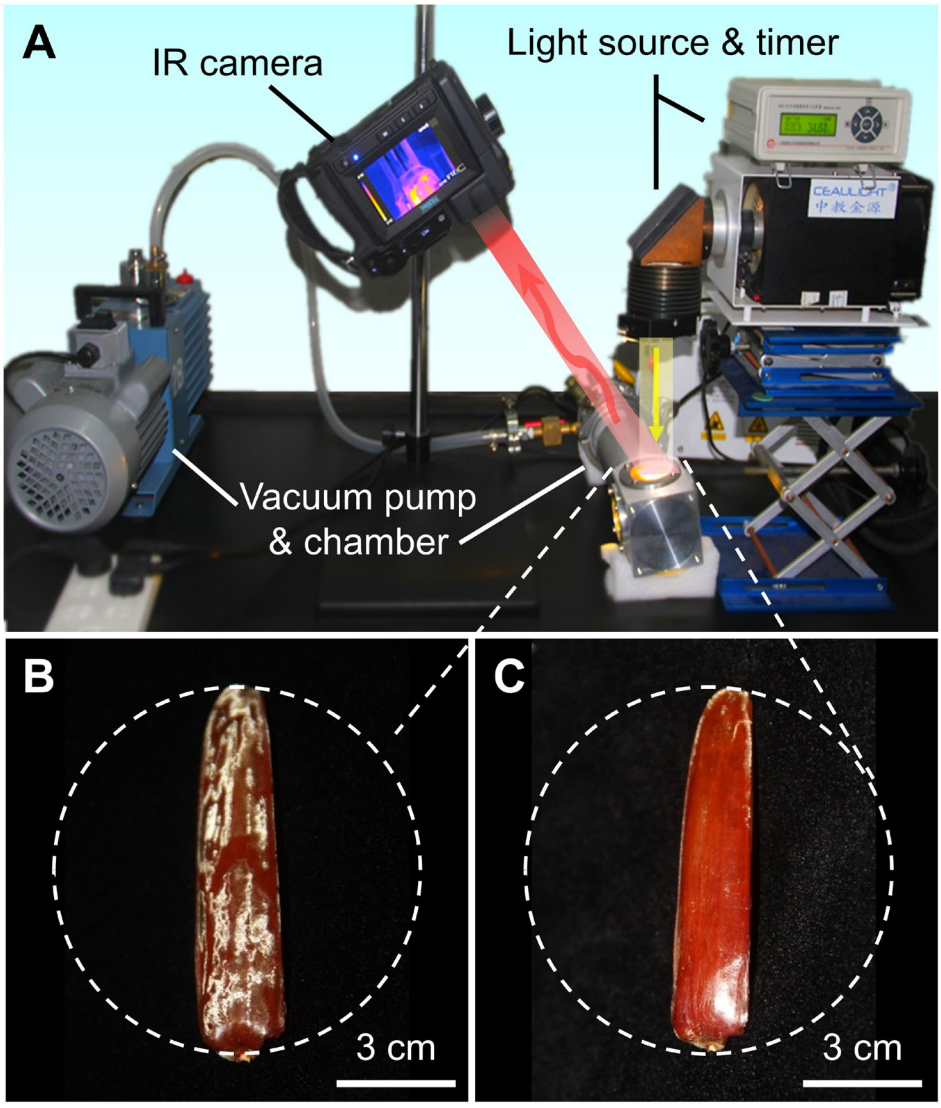

Fig. S5. Photographs of the experimental setup and the specimen. (*A*) Optical photograph of the thermodynamic experimental setup. (*B* and *C*) Photographs of the forewing before and after the fluffs removed.

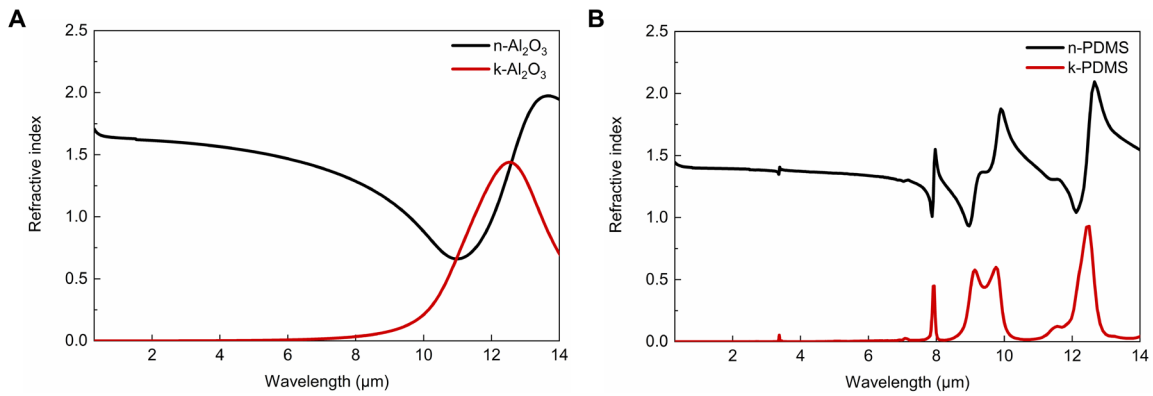

Fig. S6. The refractive index of (*A*) Al_2O_3 and (*B*) PDMS in the range of 0.3–14 μm adapted from ref (8).

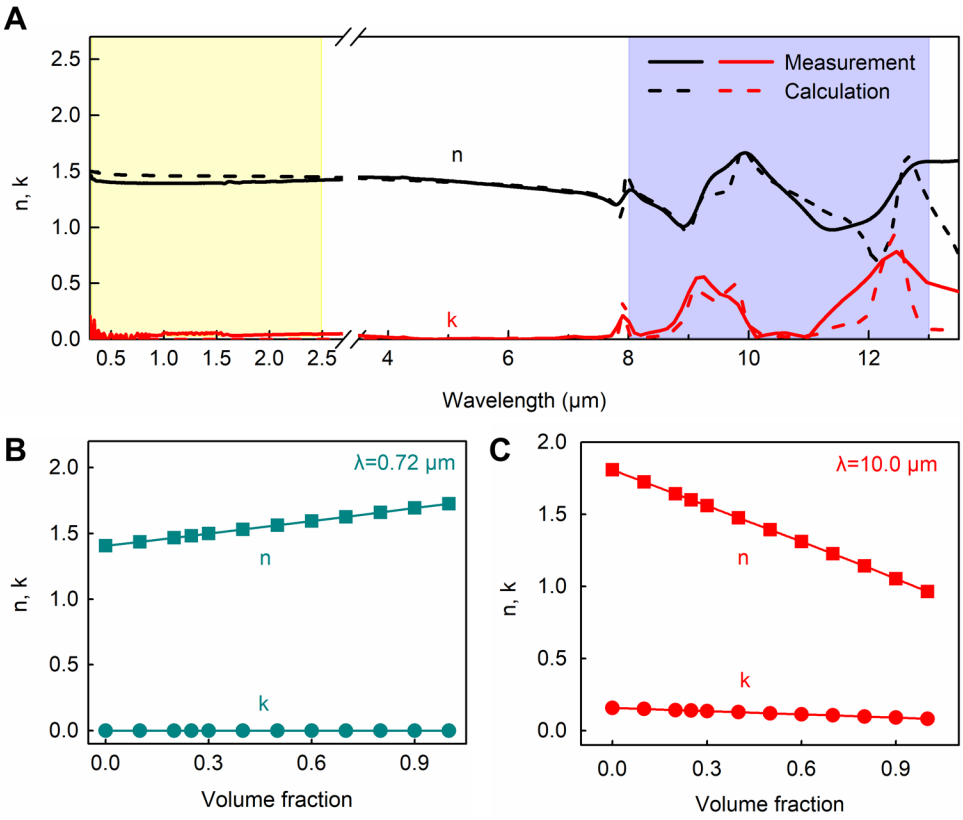

Fig. S7. Measurements and calculations of refractive index. (*A*) Theoretical calculation and experimental measurement of the refractive index of the Al_2O_3-PDMS hybrid film with a mass ratio of 1:1. (*B* and *C*) The refractive index range with the volume fraction of Al_2O_3 particles at a different wavelength in (*B*) the vis-NIR region (0.72 μm) and (*C*) the MIR region (10 μm).

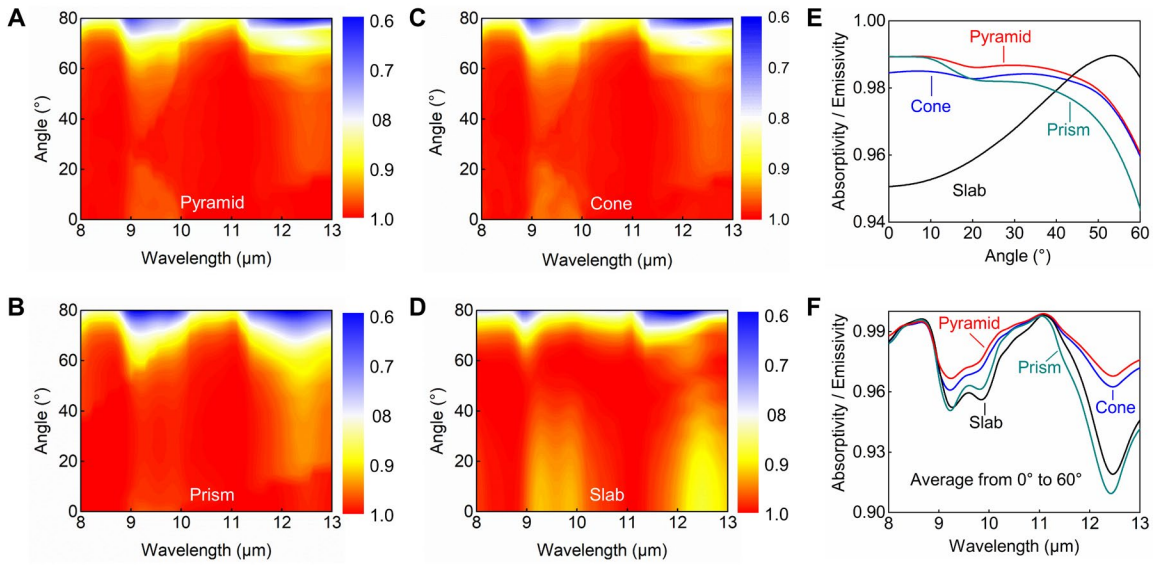

Fig. S8. Simulated optical properties of the hybrid films with different 3D morphologies. (*A*−*D*) Simulated MIR absorptivity/emissivity of the photonic films with structural arrays of (*A*) pyramid, (*B*) cone, (*C*) prism and (*D*) slab for different incident angles. (*E*) Simulated average absorptivity/ emissivity of the hybrid films with different structures in the wavelength interval of 8–13 μm varying with the incident angles. (*F*) Simulated emissivity in the range of 8–13 μm for different optimized structures with the same width and height.

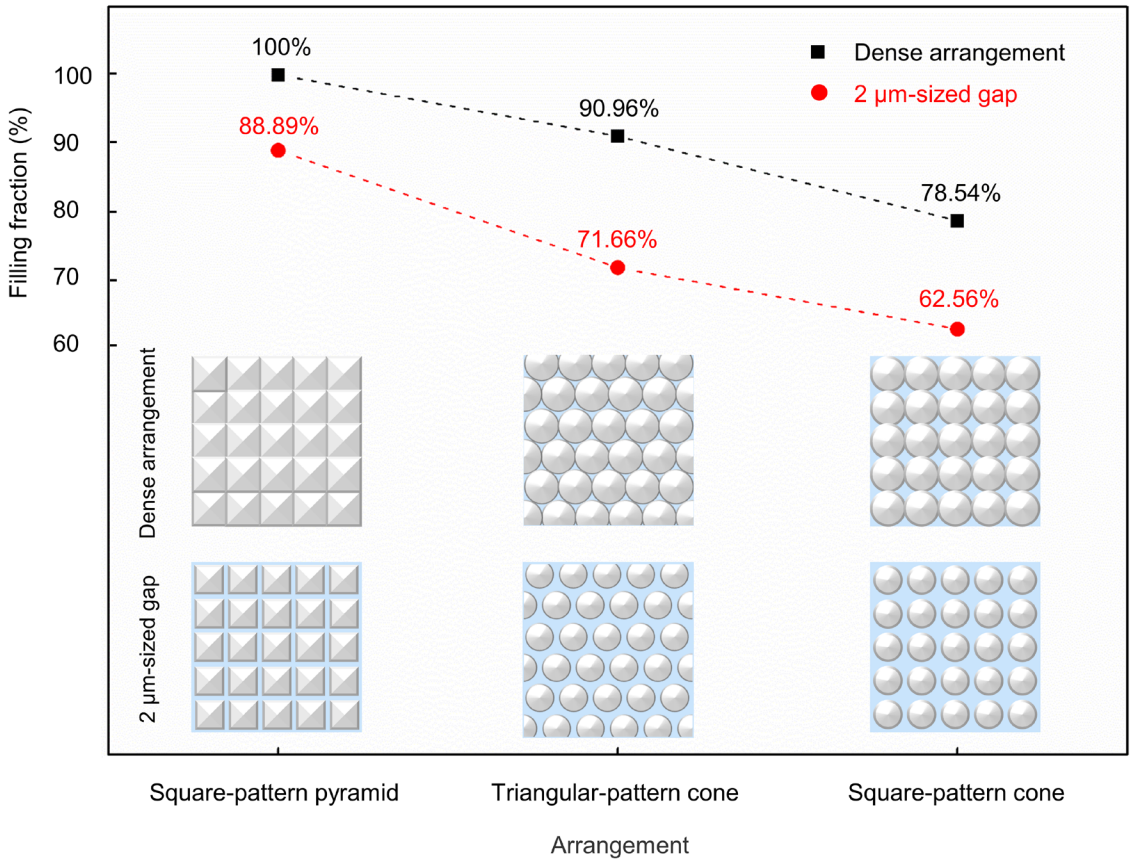

Fig. S9. Calculation of the filling fraction arranged by the square-pattern pyramids, triangular-pattern cones and square-pattern cones. The feature size of each structure array is 8 μm. The black square dots indicate the dense arrangements of different structures. The red circle dots represent the arrangements of the 2-μm-sized gap between the basic structural units.

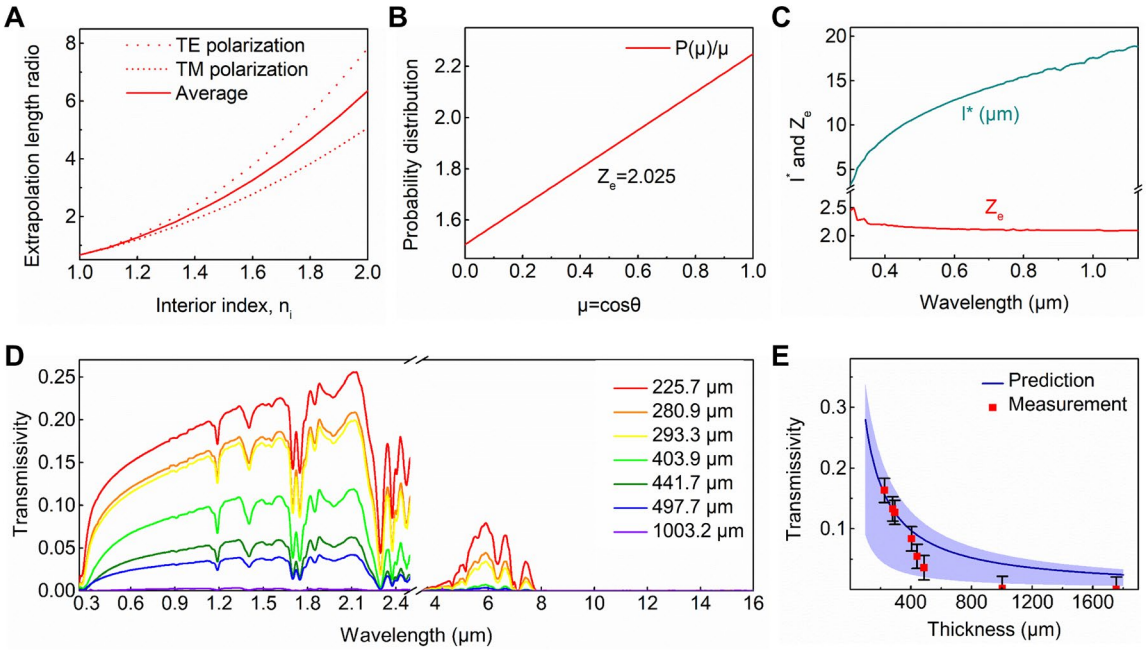

Fig. S10. Calculations based on diffusion theory and measurements of transmissivity. (*A*) Graph of extrapolation length ratio Z_e vs interior refractive index n_i predicted for samples held in air. (*B*) Graph of probability distribution $P(\mu)/\mu$ vs μ. (*C*) Calculated Z_e and mean-free path l^* for λ=0.3–1.3 μm. (*D*) Transmissivity spectra of Al_2O_3-PDMS hybrid films with different thicknesses. (*E*) Measured and computed values of spectral transmissivity (λ=0.72 μm) varying with the thicknesses. The blue region indicates the bounds of the predicted transmissivity.

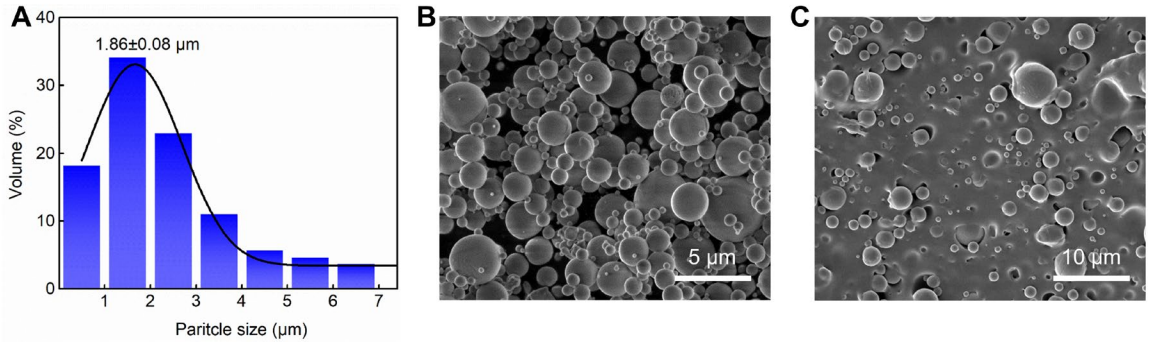

Fig. S11. Distribution of the Al_2O_3 microspheres in the PDMS matrix. (*A*) Diameter distribution of the commercial Al_2O_3 particles. (*B*-*C*) SEM images of the Al_2O_3 spherical particles (*B*) before and (*C*) after embedded into the PDMS film.

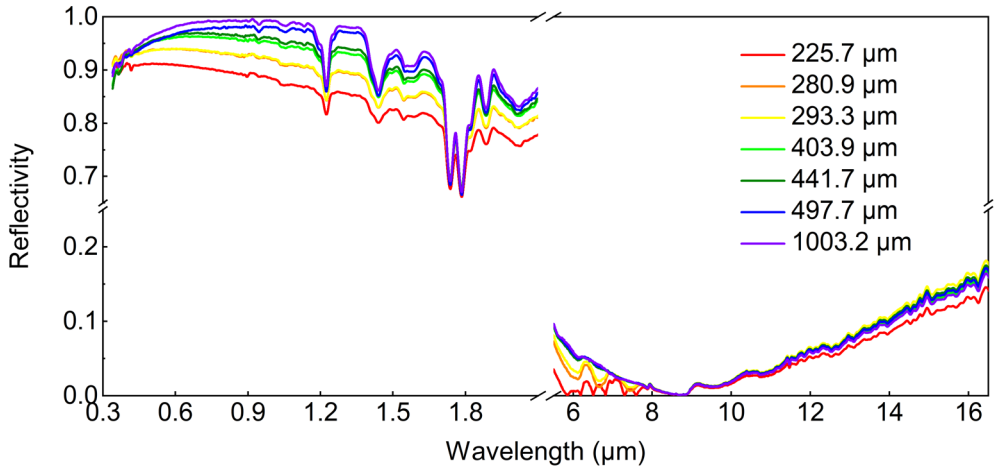

Fig. S12. Measured spectral reflectivity of the Al_2O_3-PDMS hybrid films varying with the thicknesses varying from visible to mid-infrared wavelengths.

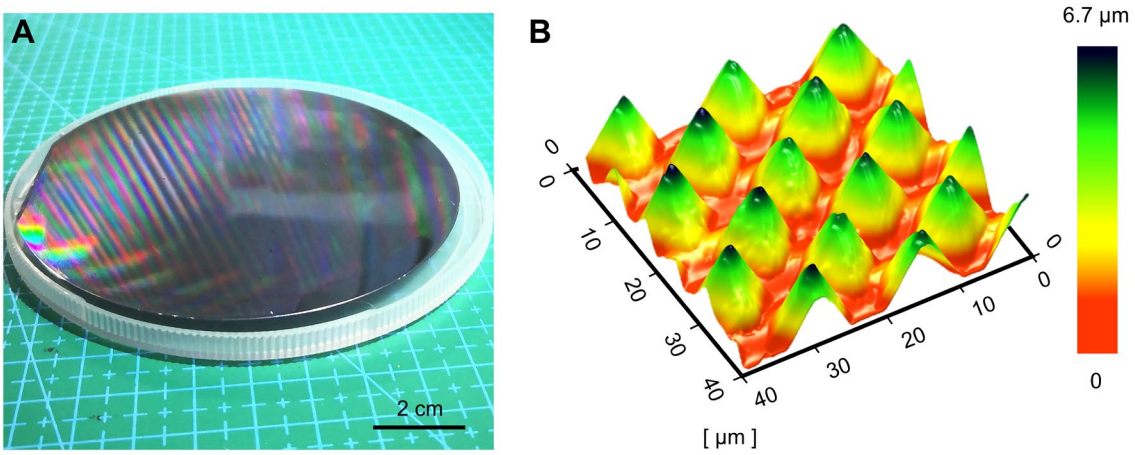

Fig. S13. Morphologies of the silicon template and the Bio-RC film. (*A*) Photograph of the silicon template. (*B*) Atomic force microscopy image of the Bio-RC film surface.

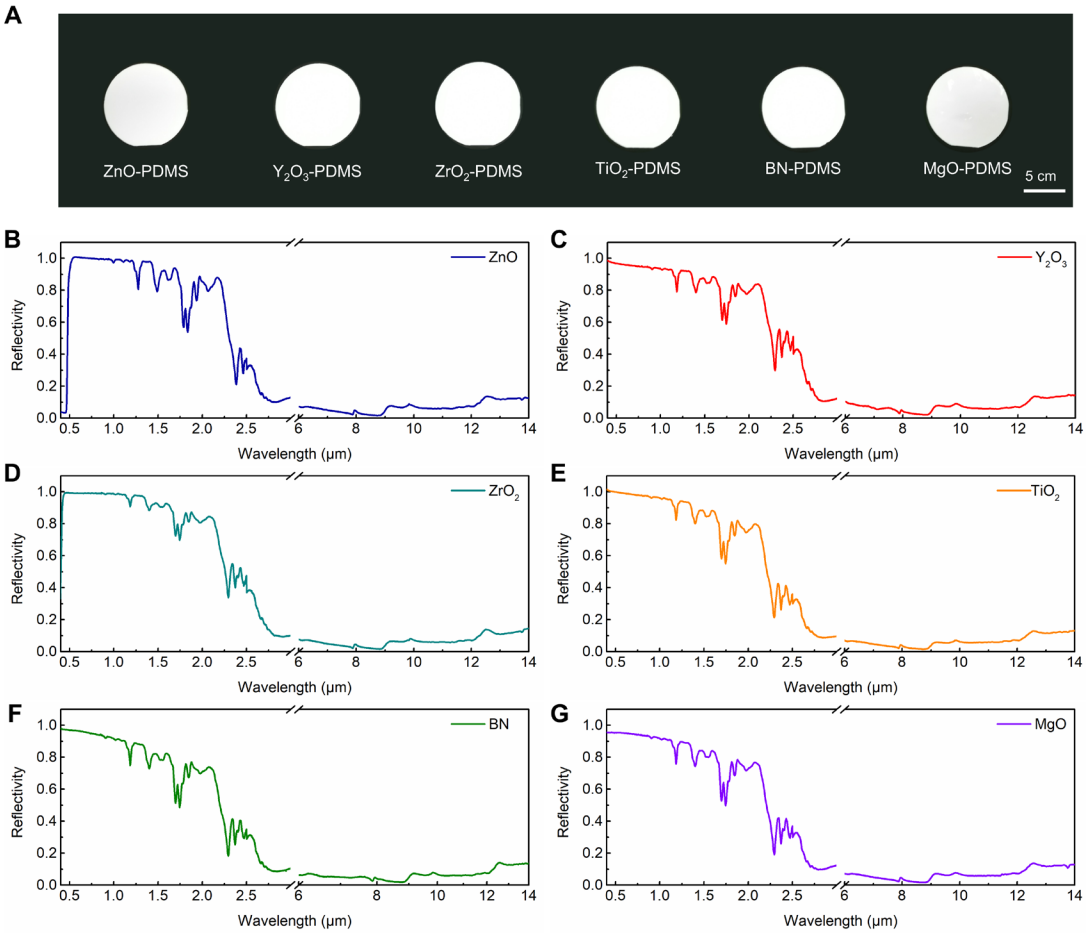

Fig. S14. Morphology and optical properties of PDMS-based photonic hybrid films embedded with different ceramic particles. (*A*) Photograph of a series of PDMS/ceramic hybrid films with photonic structures. (*B*−*G*) Measured reflectivity of the hybrid films with different ceramic particles embedded in the PDMS matrix. Reduced MIR reflectivity is consistent with enhanced emissivity based on Kirchhoff's law of thermal radiation.(9)

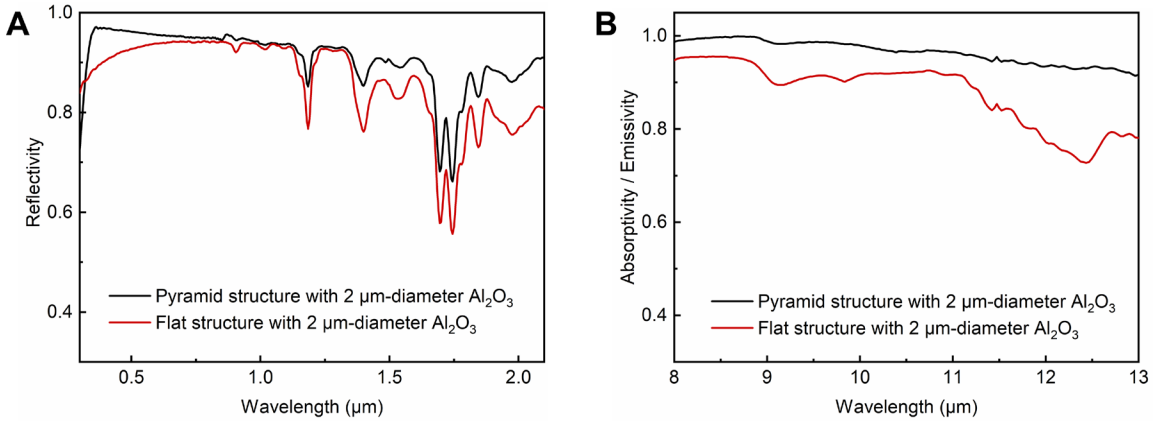

Fig. S15. Comparative optical properties between the Bio-RC film and the flat film embedded with 2 μm Al_2O_3 spherical particles. (*A*) Measured reflectivity of the films with and without micro-pyramid structure in the vis-NIR region. The enhanced reflectivity is due to the micro-pyramid arrays induced total internal reflection. (*B*) Measured emissivity of the films with and without micro-pyramid structure in the wavelength range of 8–13 μm. The MIR emissivity enhancement is because of the gradual refractive index change by the micro-pyramid arrays.

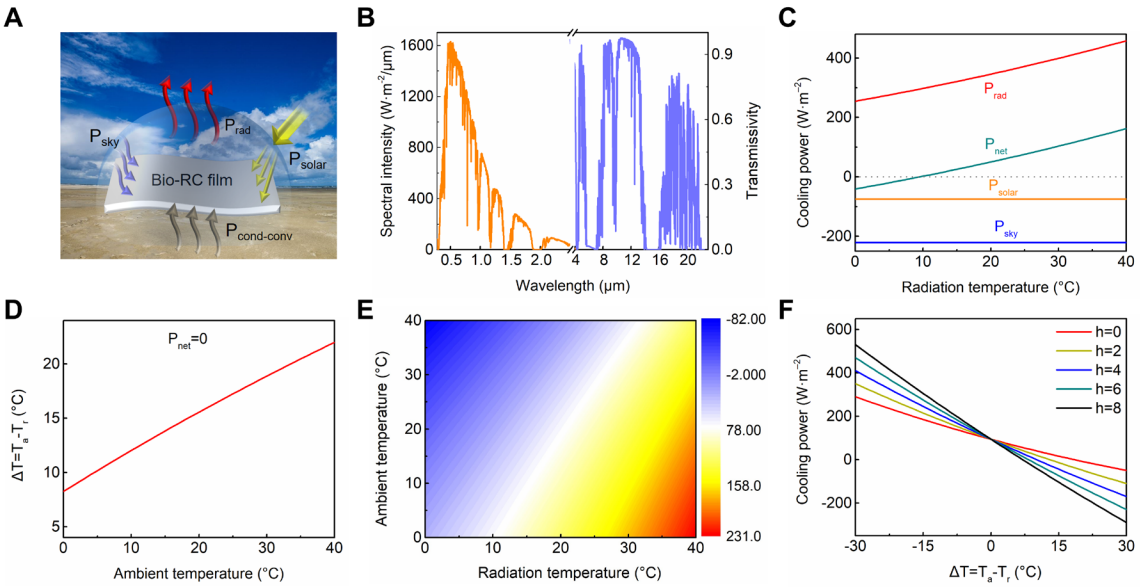

Fig. S16. Theoretical calculations of the radiation cooling performance. (*A*) Energy flow diagram of the Bio-RC film exposed to sunlight in the open air. (*B*) Spectral distribution graph of AM1.5 solar spectrum and atmospheric transmittance.(10) (*C*) Estimations of the cooling powers for an ideal Bio-RC film with the radiation temperature ranging from 0 °C to 40 °C. The non-radiative parasitic losses are assumed to be zero and the ambient temperature is fixed at 30 °C. (*D*) The maximum temperature drop ΔT as a function of the ambient temperature under the circumstance of the net radiative cooling power of zero. (*E*) Diagram of the net radiative cooling power varying with the radiation temperature and ambient temperature. (*F*) Calculations of the net cooling power P_{net} as a function of the temperature drop ΔT with different effective conductive-convective heat transfer coefficients *h*. The ambient temperature is fixed at 30 °C.

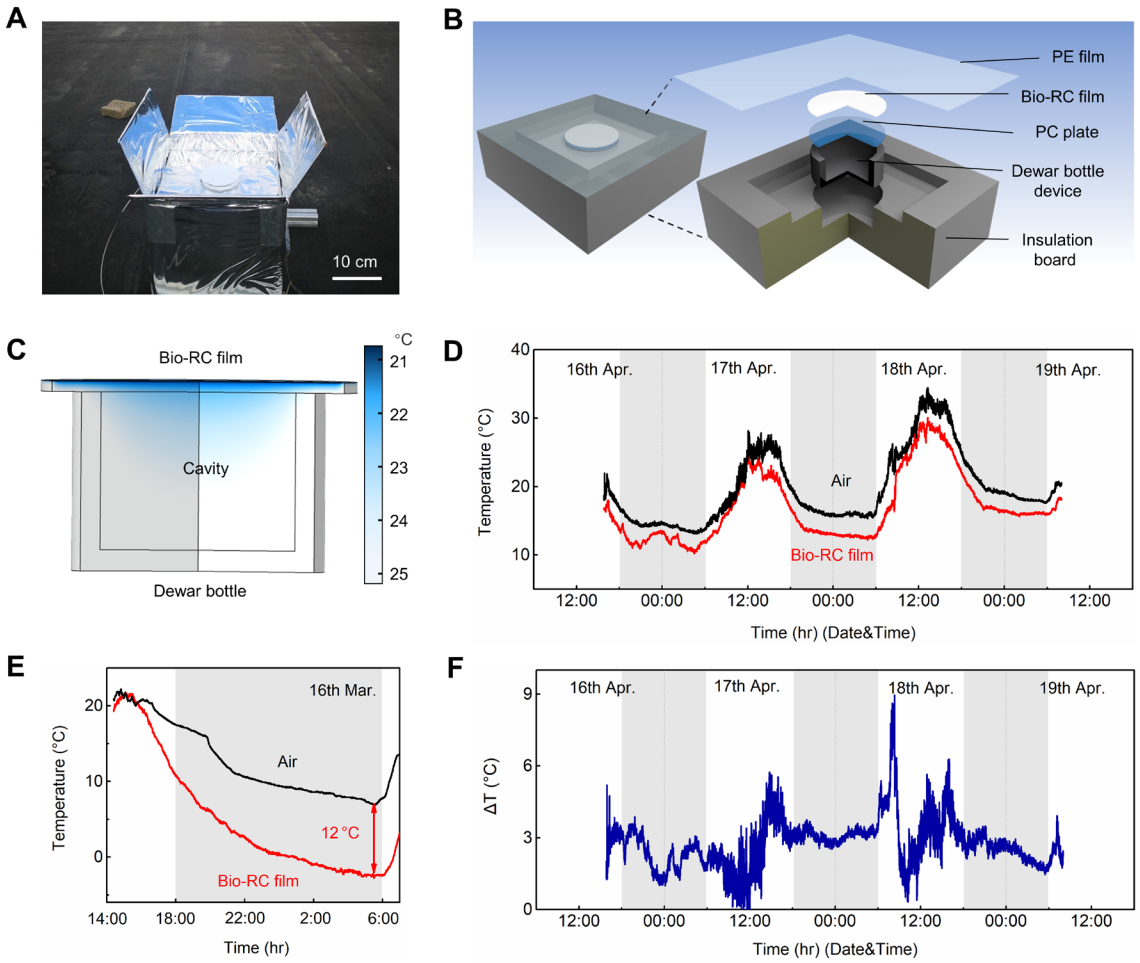

Fig. S17. Performance of the Bio-RC film for effective radiative cooling. (*A* and *B*) Photograph and schematic illustration of the cooling performance measuring setup. A Dewar bottle was covered by the Bio-RC film to insulate thermally the air. (*C*) The temperature distribution in the Dewar bottom simulated by COMSOL indicates that the air temperature gradually lowers around the film following hemispherical contours. The ambient temperature is 25 °C and the apparatus is assumed to be non-radiative heat exchange. (*D*) A 72-hour continuous temperature measurement of the Bio-RC film. The experiment demonstrated that the film could not only cool down its own body but also successfully lowered the temperature of the environment around. (*E*) Temperature variation of the air and Bio-RC film. The maximum temperature difference reached up to 12 °C. (*F*) Measured temperature difference between the Bio-RC film and the ambient air, showing an average temperature drop of 3.2 °C.

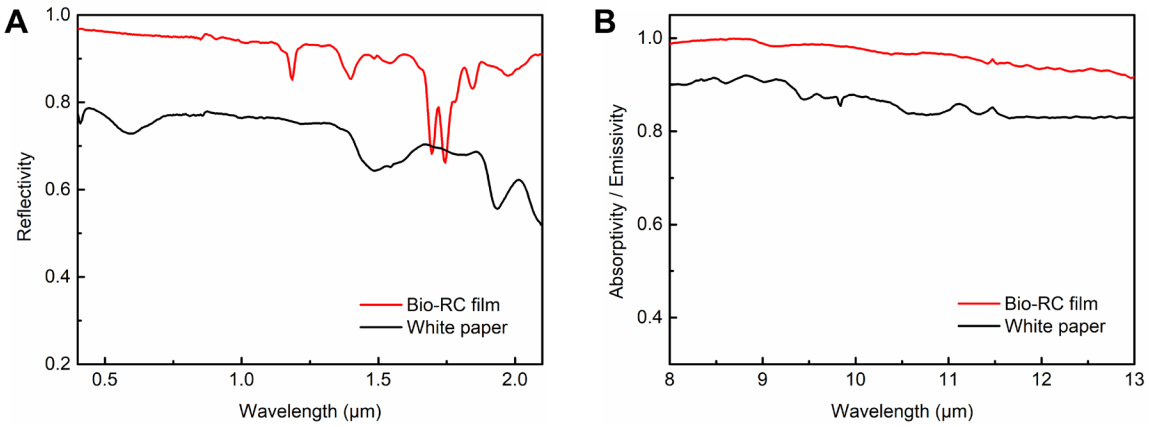

Fig. S18. Optical properties of the Bio-RC film and the white paper used in the experiment. (*A* and *B*) Measured vis-NIR reflectivity (*A*) and MIR emissivity (*B*) of the fabricated film and the white paper. The average values of the reflectivity and the emissivity of the paper are 0.72 and 0.87 respectively, which are approximately 23% in reflectivity and 9% in emissivity lower than that of the Bio-RC film.

Table S1. Thermodynamic calculation results for the forewings before and after the fluffs removal.

Conditions	Fluffy		Bald	
Mass, $m\ (g)$	0.01663		0.01602	
Surface area, $A_s\ (m^2)$	6.75×10^{-4}			
Circumstances	In air	In vacuum	In air	In vacuum
Time constant $\tau\ (s)$	5.6015	6.8995	5.7020	7.2665
$T_{max}\ (K)$	309.03	315.90	310.11	319.12
$T_{min}\ (K)$	293.77	293.39	293.76	293.35
$\overline{T}\ (K)$	301.40	304.65	301.94	306.24
MIR emissivity, ε	0.869		0.824	
Convective heat-transfer coefficient, $h\ (W/m^2 \cdot K)$	1.4651	0	1.3488	0
$\Delta Q_{rad}\ (J)$	0.05562	0.08478	0.05681	0.09352
$\Delta Q_{conv}\ (J)$	0.01509	0	0.01617	0

Table S2. Summary of successful demonstrations of passive radiative cooling and the corresponding performances.

Authors	Year	Structures/ materials	Methods	Radiative property	ΔT (°C)	P_{net} (W/m^2)	products size
This work	2019	Ceramic particles-PDMS Bio-RC film	Micro-stamping method	$R_{vis-NIR}$:95%; E_{MIR}:96%	5.1	90.8	Large scale
Li *et al.*(11)	2019	Cooling wood	Delignification and mechanical pressing	$R_{vis-NIR}$:96%; E_{MIR}>90%	4.0	53	0.2×0.2 m
Zhou *et al.*(12)	2019	Planar PDMS/metal thin film	Fast solution coating process	$R_{vis-NIR}$>90%; E_{MIR}>94.6%	2.0–9.0	76.3	Large scale
Zhao *et al.*(13)	2019	Glass-polymer hybrid metafilm	Roll-to roll	Rvis-NIR:95%; EMIR:86%	10.6	45	0.68×0.68 m
Mandal *et al.*(5)	2018	$P(VDF\text{-}HFP)_{HP}$	Phase-inversion-based method	$R_{vis-NIR}$: 96%±3%; E_{MIR}>97%±2%	6.0	96	0.15×0.15 m
Bhatia *et al.*(14)	2018	Paint-coated copper emitter	Spray painting	/	6	45	d=5 cm
Atigany-anun *et al.*(15)	2018	Silica microspheres	Colloidal sedimentation	E_{MIR}>94%	4.7	/	2.5×2.5 cm
Zhai *et al.*(16)	2017	SiO_2-TPX hybrid metamaterial	Roll-to roll	$R_{vis-NIR}$:96%; E_{MIR}>93%	/	93	Large scale
Kou *et al.*(17)	2017	PDMS/Silica/silver	Vacuum deposition	Near-blackbody in mid-infrared band	8.2	127	d=4 inch
Gentle *et al.*(18)	2015	Vikuiti enhanced specular reflector (ESR) film with silver coating	Sputter coating	$R_{vis-NIR}$:97% E_{MIR}:96%	2	70	0.19×0.19 m
Raman *et al.*(19)	2014	SiO_2/HfO_2/metal	Electron beam evaporation	$R_{vis-NIR}$:97% E_{MIR}:~0.65	4.9	~40.1	d=0.2 m

Movie S1. The drying cycle of the wetting and drying experiment.

Movie S2. The water resistance experiment and potentially self-cleaning behavior of the Bio-RC film

SI References

1. D. H. Raguin, G. M. Morris, Analysis of antireflection-structured surfaces with continuous one-dimensional surface profiles. *Applied optics* **32**, 2582-2598 (1993).
2. N. N. Shi *et al.*, Keeping cool: Enhanced optical reflection and radiative heat dissipation in Saharan silver ants. *Science* **349**, 298-301 (2015).
3. A. R. Gentle, G. B. Smith, Radiative heat pumping from the Earth using surface phonon resonant nanoparticles. *Nano letters* **10**, 373-379 (2010).
4. B. Czapla, A. Srinivasan, Q. Yin, A. Narayanaswamy (2017) Potential for Passive Radiative Cooling by PDMS Selective Emitters. in *ASME 2017 Heat Transfer Summer Conference*.
5. J. Mandal *et al.*, Hierarchically porous polymer coatings for highly efficient passive daytime radiative cooling. *Science* **362**, 315-318 (2018).
6. Vera, Durian, Angular distribution of diffusely transmitted light. *Physical review. E, Statistical physics, plasmas, fluids, and related interdisciplinary topics* **53**, 3215-3224 (1996).
7. B. Zhao, M. Hu, X. Ao, N. Chen, G. Pei, Radiative cooling: A review of fundamentals, materials, applications, and prospects. *Applied Energy* **236**, 489-513 (2019).
8 M. N. Polyanskiy (Accessed 12th Oct 2018) Refractive index database. in *Available at: https://refractiveindex.info*.
9. R. Siegel, *Thermal Radiation Heat Transfer, Fourth Edition* (2001).
10. G. Observatory (Accessed 1th Dec 2018) IR Transmission Spectra. in *Available at: http://www.gemini.edu/sciops/telescopes-and-sites/observing-condition-constraints/ir-transmission-spectra*.
11. T. Li *et al.*, A radiative cooling structural material. *Science* **364**, 760-763 (2019).
12. L. Zhou *et al.*, A polydimethylsiloxane-coated metal structure for all-day radiative cooling. *Nature Sustainability* **2**, 718-724 (2019).
13. D. Zhao *et al.*, Subambient Cooling of Water: Toward Real-World Applications of Daytime Radiative Cooling. *Joule* **3**, 111-123 (2019).
14. B. Bhatia *et al.*, Passive directional sub-ambient daytime radiative cooling. *Nature communications* **9**, 5001 (2018).
15. S. Atiganyanun *et al.*, Effective Radiative Cooling by Paint-Format Microsphere-Based Photonic Random Media. *ACS Photonics* **5**, 1181-1187 (2018).
16. Y. Zhai *et al.*, Scalable-manufactured randomized glass-polymer hybrid metamaterial for daytime radiative cooling. *Science* **355**, 1062-1066 (2017).
17. J.-I. Kou, Z. Jurado, Z. Chen, S. Fan, A. J. Minnich, Daytime Radiative Cooling Using Near-Black Infrared Emitters. *ACS Photonics* **4**, 626-630 (2017).
18. A. R. Gentle, G. B. Smith, A Subambient Open Roof Surface under the Mid-Summer Sun. *Advanced science* **2**, 1500119 (2015).
19. A. P. Raman, M. A. Anoma, L. Zhu, E. Rephaeli, S. Fan, Passive radiative cooling below ambient air temperature under direct sunlight. *Nature* **515**, 540-544 (2014).